Exploring the structure evolution of MoS_2 upon Li/Na/K ion insertion and origin of unusual stability for potassium ion batteries

Xiaoqiong Du[1,‡], Xuyun Guo[1,‡], Jiaqiang Huang[1,‡], Ziheng Lu[3], Hong Tan[1,2], Jian-Qiu Huang[1], Ye Zhu[1,*], Biao Zhang[1,2,*]

1. Department of Applied Physics, Research Institute for Smart Energy, The Hong Kong Polytechnic University, Hung Hom, Hong Kong, China

2. The Hong Kong Polytechnic University Shenzhen Research Institute, Shenzhen 518063, China

3. Shenzhen Institutes of Advanced Technology, Chinese Academy of Sciences, Shenzhen 518055, China

‡ These authors contributed equally.

* Email: ye.ap.zhu@polyu.edu.hk; biao.ap.zhang@polyu.edu.hk.

Abstract

The recent revival of the research on Na, K ion batteries have twofold benefits. It not only provides alternative energy storage technologies to Li ion batteries with potential advantages on the cost but also enhances our understanding of charge storage through systematic studies on alkali-metal ion batteries with increasing insertion ion sizes. Using MoS_2 as a model material, the structure evolution upon Li, Na, and K ions uptake are compared through *in situ* TEM. Despite the larger size, K ions insertion shows better both electrochemical and structural stability. To understand this paradoxical and counter-intuitive phenomenon, *in situ* XRD are carried out to examine the phase transitions of MoS_2 upon the ion insertion, while *ex situ* TEM are further applied to have a close look at the structures at the nanoscale. Complementary DFT calculations are performed to understand the kinetic/thermodynamic origins of the analogous stability. It reveals that the less electrovalent K-S bond favors the intercalation process, resulting in the preservation of layered structure for stable cycling. This study provides structural insight to design stable electrodes for K-ion batteries.

Graphical abstract

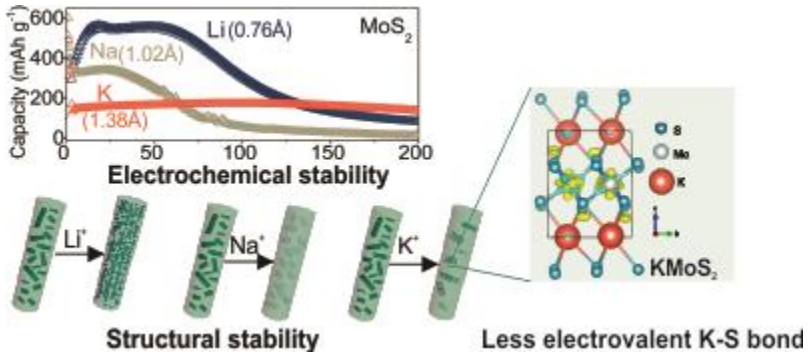

Keywords

MoS_2 nanofibers, *in situ* TEM, structure evolution, DFT calculations, potassium ion batteries

New concepts

Two-dimensional layered MoS_2 is among the most promising anode materials for alkali-metal ion batteries due to the high theoretical capacity and large interlayer spacing. However, inferior cyclic performance caused by structure collapse limits its wide applications. It is generally believed that severer capacity degradation associated with extensive volume expansion shall occur for K ion batteries because of its large ion radius. An unusual stability is observed during the insertion of larger sized K ion than Na and Li ions, which differs from other anode materials like Sb or Bi. With the help of *in/ex situ* TEM and *in situ* XRD, we reveal the different reaction mechanisms of MoS_2 upon Li/Na/K ions. The conversion reaction (destroying layered structure) is inclined to take place after Li-ion inserting, while the intercalation reaction (maintaining layered structures) dominates the K ion uptake. The origin of this abnormal phenomenon is unveiled by the complementary DFT simulation, which shows the suppression of conversion reaction owing to the less electrovalent of K-S bond. Our findings demonstrate that the charge radius does not directly determine the battery stability, and the reaction pathway also plays a critical role.

Introduction

The advantages of Li ion batteries (LIBs) over other metal ion systems rely on both the low redox potential of Li^+/Li (-3.04 V vs. SHE) and the small size of Li ion (0.76 Å).[1] With the concerns about the sustainability of lithium sources, researches on sodium and potassium-based technologies have been revived considering the close redox potential of Na^+/Na (-2.71 V vs. SHE) and K^+/K (-2.94 V vs. SHE), which would enable the design of high-output-voltage batteries.[2, 3] Similarities between alkali-metal ions are expected to smooth the development as the knowledge on LIBs that accumulated in the past three decades can be largely applied to the Na ion batteries (SIBs) and K ion batteries (PIBs).[4, 5] Indeed, analogous systems from the electrolytes to electrode materials are adopted in the alkali-metal ion batteries. For instance, carbonate-based solvents, including ethylene carbonate (EC), dimethyl carbonate (DMC) and diethyl carbonate (DEC) inherited from LIBs remain the most popular choices for the electrolytes in SIBs and PIBs.[6-10] Many materials are capable of storing all the Li, Na and K ion, with hard carbon anode and $A_3V_2(PO_4)_2F_3$ (A represents Li, Na or K) cathode being the representatives.[11-16] Nevertheless, a simple extrapolation from Li to Na, K system is undoubtedly not enough. This is clearly reflected in the case of $LiCoO_2$, the most successful cathode in LIBs, whose Na_xCoO_2 and K_xCoO_2 counterparts fail to deliver attractive capacity and stability.[17, 18] While the reasons for the varieties are complex, the large ionic size of Na (1.02 Å) and K (1.38 Å) ion is considered partly responsible. Uptake of ions with a large radius would lead to enormous volume expansion and bring about potential structural damage to the electrode materials. An example is the alloy anodes, which can accept several A ions to form A_xM (A represents Li, Na or K, and M denotes alloy anodes such as Bi and Sb); much more significant volume expansion is induced in the formation of K_xM than Li_xM and Na_xM.[19, 20] Consequently,

stabilizing electrodes in PIBs is considered more challenging, necessitating the efforts on both microstructure design and solid electrolyte interphase engineering.[21-23]

Comparison studies between alkali-metal ion storage are expected to shed insights into the effect of ionic carriers on the structural evolution of electrodes, which are somewhat lacking due likely to the absence of appropriate host materials. MoS_2 has a large layered distance of 6.3 Å, making it an ideal material to accommodate alkali-metal ions with different sizes. It shows promising theoretical capacities of about 670 mA h g^{-1} *via* a four-electrons-transfer reaction when serving as the anode in LIBs, SIBs, and PIBs.[24-30] Similar charge storage mechanisms are reported, including the intercalation at a high voltage to form layered $AMoS_2$ (**Equation 1**) compounds and the following conversion reaction to precipitate molybdenum metal and A_2S (**Equation 2**).[31-33] Herein, we fabricated MoS_2/C nanofibers as a model material considering the advantages of one-dimensional morphology for *in situ* experimental and statistics gathering. It reveals that MoS_2/C nanofibers in PIBs shows the largest volume expansion up to 140%, whereas the volume changes in LIBs and SIBs are only about 103% and 123%, respectively. Counter-intuitively, better structural stabilities and more stable cyclic performance during K ion insertion are observed. Complementary *in/ex situ* transmission electron microscopy (TEM) and theoretical calculations were conducted to study the origin of the difference in structural transformations during Li, Na, and K ions insertion.

$$MoS_2 + A \rightarrow AMoS_2 \quad (1)$$

$$AMoS_2 + 3A \rightarrow Mo + 2A_2S \quad (2)$$

where A represents Li, Na or K.

Results and Discussion

MoS_2/C nanofibers were prepared by electrospinning (**Figure S1**). The crystalline phase of the nanofibers is identified by X-ray powder diffraction (XRD, **Figure S2**a), which is consistent with 2H-MoS_2 (PDF#37-1492). A sharp peak at around 14.1 ° can be indexed to (002) plane of MoS_2 and one broad peak at about 21.2 ° belongs to carbon that originated from carbonization of PAN. The thermogravimetry (TG, **Figure S2**b) is performed to analyze carbon content in the sample, which is estimated to be ~25%. The chemical state of Mo is examined by X-ray photoelectron spectroscopy (XPS, **Figure S3**), which present two pairs of peaks at 229.0 eV and 232.3 eV in Mo3d spectrum, corresponding to Mo(Ⅳ) and Mo (Ⅵ) respectively. The small amount of Mo (Ⅵ) species in Mo3d spectrum may originate from the oxide layer of the MoS_2/C nanofiber. [Ref] The morphologies of MoS_2/C nanofibers are investigated by scanning electron microscopy (SEM) and TEM. In **Figure S4**a, the MoS_2/C nanofibers with an average diameter of about 100 nm present uniform thread morphologies after high-temperature treatment. TEM images (**Figure S4**b and c) indicate that layered MoS_2 crystals are homogeneously dispersed in the carbon nanofibers and the selected area electron diffraction (SAED) pattern (**Figure S4**b inset) clearly shows the multi-crystalline feature of MoS_2. In the high-resolution (HRTEM) images (**Figure S4**d), MoS_2 crystals consist of 3-5 layers with an interlayer distance of 6.3 Å.

In situ TEM examinations were carried out to explore the charge storage processes of MoS_2/C nanofibers uptake of different alkali-metal size ions with alkaline oxides on the surfaces as solid electrolytes and the alkaline metal as the reference/counter electrodes (**Figure S5**). As shown in **Figure 1**a and b, after the first 10 seconds of lithiation and sodiation, the interlayer spacing of MoS_2 increases from 6.3 Å to about 6.4 Å and 7.0 Å, respectively. While for the potassiation process, the interlayer spacing is enlarged to a striking 7.9 Å (**Figure 1**c). Despite the expansions of layers distance by the alkaline atom invasion, the lamellar structure can be retained well in

three types of batteries. These processes are mainly involved with the intercalation reaction that alkaline ions are inserted into MoS_2 to form layered $AMoS_2$ compounds, namely, $LiMoS_2$, $NaMoS_2$, and $KMoS_2$, respectively.[37-40] As for a deep reaction in in the following 12 seconds, the layered crystals have almost entirely disappeared in the cases of lithiation because of the conversion of $LiMoS_2$ to metallic Mo and Li_2S. Some of the layered crystals are preserved during Na insertion, but the MoS_2 crystals are broken into small pieces. In comparison, the deep potassiation process of MoS_2 displays a different phenomenon from the Li and the Na counterparts that the layered crystals are unabridged with an enlarged interlayer spacing of 7.9 Å. *In situ* TEM movies of these three processes are given in supporting information (Movie S1-3). Electron energy loss spectroscopy (EELS) maps (**Figure S**6-S8) confirm that Li, Na and K are successfully inserted into MoS_2/C nanofibers. The lattice width of MoS_2 crystals and the lateral length of MoS_2/C nanofibers are measured in real time and the detailed statistics are given in **Figure 1**d and e. The expansion of interlayer distance becomes more severe with the increase of intercalant size from Li to Na and K ions. Correspondingly, the lateral expansion of nanofibers after taking Li and Na ions is roughly calculated to be 103% and 123%, respectively, while it reaches nearly 140% for K ions uptake.

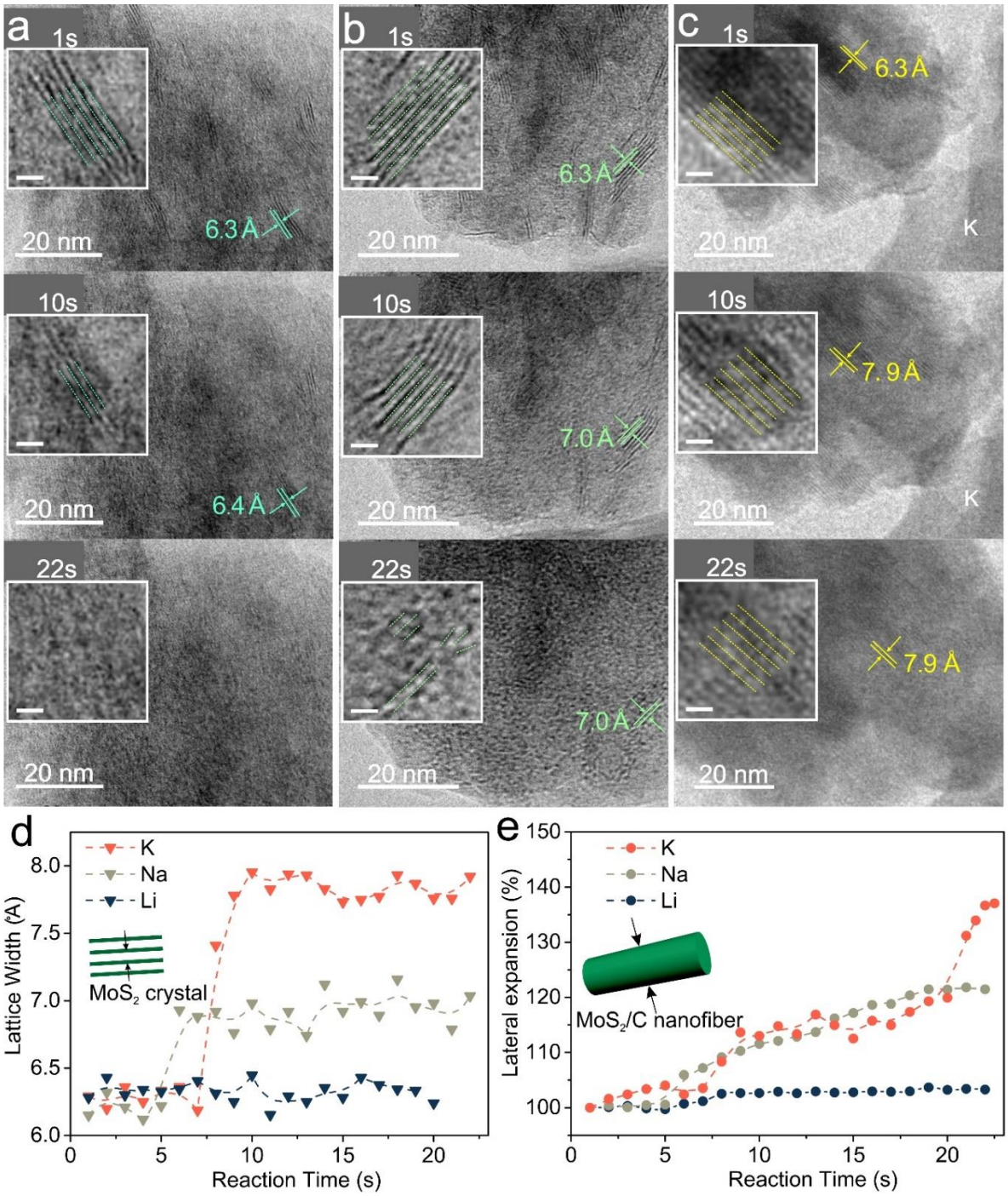

Figure 1. *In situ* TEM images of MoS_2/C nanofibers for (a) Li^+, (b) Na^+ and (c) K^+ uptake at different reaction stages (insets: magnified images with a scale bar of 2 nm). The statistic scatters diagram of (d) lattice width of MoS_2 crystal and (e) lateral expansion of MoS_2/C nanofiber in real-time *in situ* TEM observations.

To exclude potential artifacts from *in situ* TEM setup, such as the use of A_2O solid electrolytes, we further performed *in situ* XRD and *ex situ* TEM on real LIBs, SIBs and PIBs, to investigate the unexpected structural stability of MoS_2 at various Li/Na/K ions insertion/extraction stages. The *in situ* XRD patterns of MoS_2/C nanofibers for K ion storage in the first and second cycles are presented in **Figure 2**a. During the first discharging process, the intensity of the MoS_2 peak located at 14.1 ° gradually decreases and a new peak at about 10.6 ° becomes more prominent, which can be assigned to $K_{0.4}MoS_2$ compound (PDF#27-0421). Then $K_{0.4}MoS_2$ peak shifts to 11.1 ° after continuous K ions interpolation, where the formed compound is defined as K_xMoS_2 ($x>0.4$). Further insertion of K ions leads to the fully potassiated phase $KMoS_2$ pertaining to a broad peak at 11.3 °, which agrees well with the 7.9 Å interlayer spacing observed in TEM. Turning to the charging processes, the wide peak of 11.3 ° shifts back to 11.1 ° and no obvious MoS_2 peaks emerge, indicating that $KMoS_2$ can only return to K_xMoS_2 ($0.4<x<1.0$) instead of pristine MoS_2. For the following discharging and charging processes, only $KMoS_2$ and K_xMoS_2 appear on the stage and the corresponding XRD peaks show a periodic right and left shifts. The K ions shuttle between K_xMoS_2 and $KMoS_2$ assures that the phase transition is completely reversible in cycles. It should be noted that the interlayer spacing of K_xMoS_2 shrinks during K ion insertion, while it extends when K ion extraction. This inverse relationship between the interlayer spacing and K ion insertion/extraction can be explained by the 2H-1T phase transformation.[41-43] In the case of LIBs (**Figure S9**a), the peak of (002) facet gradually shifts to 13.7 º after Li ion insertion, which can be attributed to the intercalated product-$LiMoS_2$.[43] When discharging to 0 V, no obvious peaks can be recognized, indicating the MoS_2 is transformed to small sized/amorphous Mo and Li_2S.[44] When charging back to 3 V, no MoS_2 peaks are founded, which means the layered structures of MoS_2 are largely vanished and cannot be recovered after

Li ion insertion/extraction. In first discharging process of SIBs (**Figure S9**b), two new peaks at 11.7 º and 12.5 º are observed, corresponding to $Na_{0.5}MoS_2$ and $NaMoS_2$ species, respectively.[33] After fully discharge to 0 V, most of the layered $NaMoS_2$ are decomposed suggested by the low intensity of the peak at 12.5 º. It shows the similar phenomena with Li case that no peaks can be found at fully charged 3 V, implying an amorphous or negligible crystallized MoS_2 are recovered after Na ion insertion/extraction.

The above *in situ* observations are fully consistent with *ex situ* TEM characterizations on the first cycle of real PIBs. The pristine MoS_2 crystals in the nanofiber are shown in **Figure S10**a and b. When discharging to 1.0 V, a large interlayer spacing of 8.3 Å associated with $K_{0.4}MoS_2$ is observed (**Figure S10**c and d), corresponding to the 10.6 ° peak in *in situ* XRD. However, it is not probed by *in situ* TEM probably due to the low-resolution limitation in real time observation and fast reaction process of $K_{0.4}MoS_2$.[45] After discharging to 0.5 V (**Figure S10**e and f), a slightly shrunken layer distance of 8.0 Å can be found arising from 2H-1T phase transformation, which is related to the 11.1° peak from K_xMoS_2 according to *in situ* XRD results. Some unreacted MoS_2 can be seen with the original interlayer distance of 6.3 Å. For the fully discharged state (**Figure S10**g and h), most of MoS_2 are converted to $KMoS_2$ with a contractive distance of 7.9 Å, as observed by both *in situ* TEM and XRD. Back to 3 V (**Figure S10**i and j), the interlayer distance is extended again to 8.0 Å, indicating that $KMoS_2$ backtrack to K_xMoS_2 species. Thanks to statistic advantage of nanofiber composite that the MoS_2 crystals are scattered in nanofibers independently, the layer numbers and lateral length can be readily measured. As shown in **Figure 2b**, the layer numbers of MoS_2 crystal in nanofibers at different states are counted. The original MoS_2 presents 3-5 layers, which almost does not change upon

charge/discharge, confirming the stability of the layered crystals and the reversible reaction between $KMoS_2$ and K_xMoS_2.

Ex situ TEM characterizations were also carried out on LIBs and SIBs at the fully discharged state, to be compared with PIBs. As shown in **Figure 2**d and inset, only dense Mo particles with the lattice-plane spacing of 2.2 Å (PDF#42-1120) are discovered in discharged LIBs, with no trace of layered phases, implying that deep conversion dominates. The small sized metallic Mo may be nondetectable in *in situ* XRD. A small number of layered crystals are presented in discharged SIBs (**Figure 2**e), which are smaller and contain fewer layers with an expanded interlayer spacing of 7.0 Å, in agreement with the *in situ* TEM and *in situ* XRD observation in **Figure 1**b. In contrast, many broad layered crystals with a large interlayer spacing of 7.9 Å are preserved in discharged PIBs (**Figure 2**f). The lateral lengths of layered crystals in both SIBs and PIBs are counted at fully discharged state (**Figure 2**c). The average lateral length of pristine MoS_2 crystals in nanofibers is about 5.2 nm. This value in SIBs dramatically decreases to ca 3.4 nm after sodiation. Those layered crystals vanished in LIBs and SIBs have been presumably converted to Mo and Li_2S/Na_2S species through conversion reactions. On the other hand, the lateral length (4.9 nm) in PIBs does not show significant change after discharging to 0 V, further proving the better stability of the layered crystals during K ion storage.

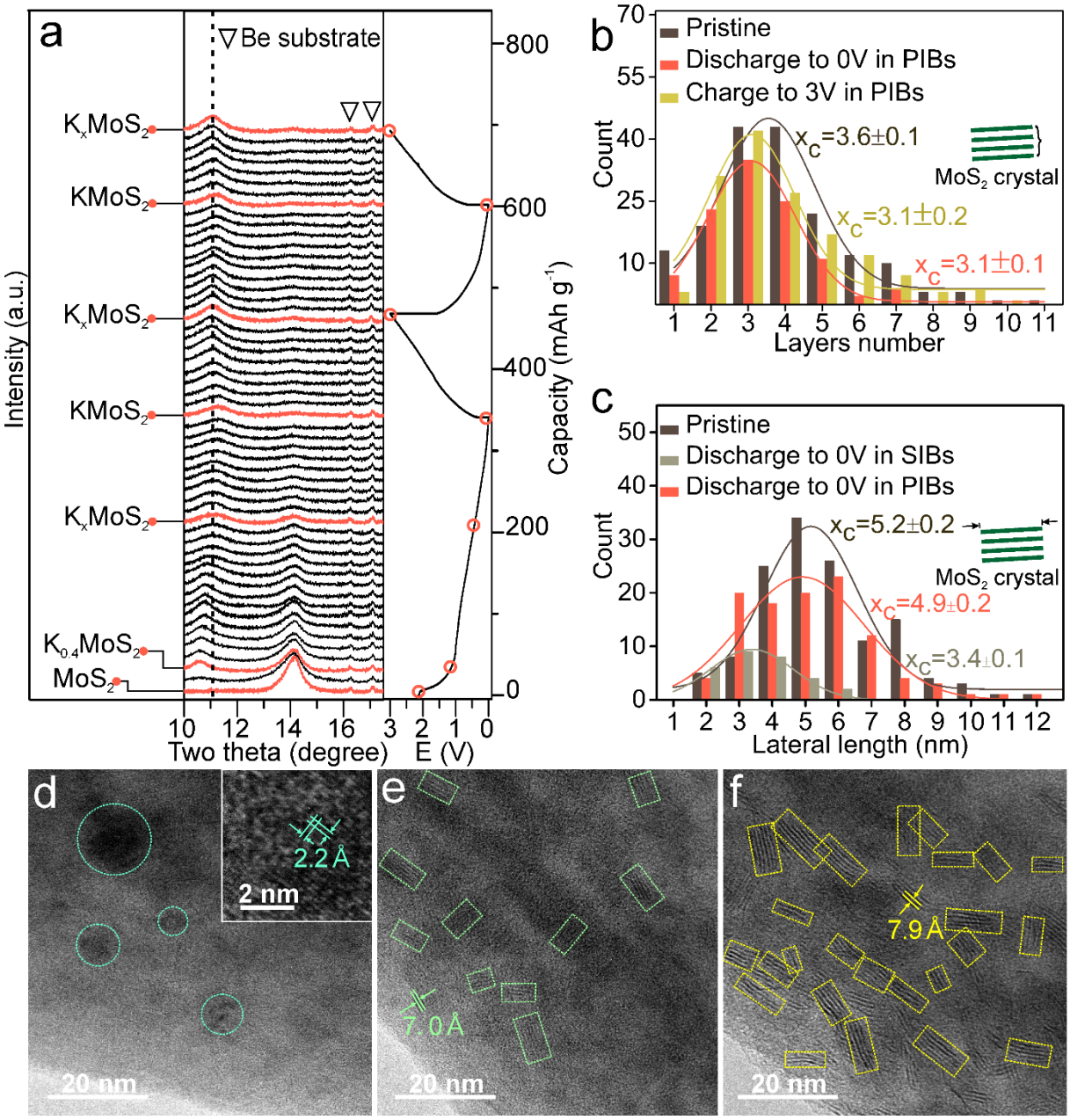

Figure 2. *In situ* XRD and *ex situ* TEM for MoS_2/C nanofibers. (a) In situ XRD patterns in PIBs in the first two cycles; The statistic histograms for MoS_2 crystals of (b) layer numbers at different states in PIBs and (c) lateral length in PIBs and SIBs; *Ex situ* TEM images at first fully discharged state in (d) LIBs; (e) SIBs and (f) PIBs (Conversion reaction products in LIBs are marked by circles and intercalation reaction products in SIBs and PIBs are marked by rectangles).

The electrochemical performances of MoS_2/C nanofibers were tested in LIBs, SIBs, and PIBs for exploring the consequences of structural transformation on the cyclic stability. The first discharge and charge profiles of MoS_2/C nanofibers in LIBs, SIBs, and PIBs are compared in **Figure 3**a. Much longer plateaus are observed in LIBs and SIBs, indicative of the distinct reaction paths. It can be seen more clearly in dQ/dV plots where sharp peaks are presented during Li and Na insertion (**Figure 3**b). Consistent with the observed structural stability, MoS_2/C nanofibers demonstrate the most stable behavior in PIBs, with a capacity retention of about 99.4% after 200 cycles (**Figure 3**c and d). MoS_2/C nanofibers presents a good rate performance for PIBs (**Figure S11**), which is not affected by the larger radius of K ion, showing reversible capacities of 212, 196.2, 186.4, 175.2 mA h g^{-1} under increasing current density of 50, 100, 200 and 400 mA h g^{-1}, respectively. Note that the pure carbon nanofibers have a capacity of mere 100 m A h g^{-1} (**Figure S12**). Considering the 75 wt.% mass loading of MoS_2 in the composite, the MoS_2 alone in the composite delivers a capacity of about 200 m A h g^{-1} at the high current density of 500 m A g^{-1}. In contrast, relatively rapid capacity decreases are observed in LIBs and SIBs, retaining only 80.1% and 70.1% of the initial capacity, respectively. As is well-known, the carbon host in the nanofibers would conduce to better cycling performance for active materials.[46-48] To exclude the interference of carbon, petal-like neat MoS_2 was synthesized by the hydrothermal method. As shown in **Figure S13**a, the prepared neat MoS_2 presents a pure 2H-MoS_2 phase (PDF#37-1492) without any carbon signal. In TEM images (**Figure S13**b, c and b inset), neat MoS_2 present petal-like morphologies with a diameter of ca. 200 nm and are polycrystalline, as revealed by SAED. The HRTEM image (**Figure S13**d) clearly displays a layered structure with an interlayer spacing of 6.3 Å, which is the same as the MoS_2/C nanofibers. The cyclic performances of neat MoS_2 in LIBs, SIBs and PIBs are given in **Figure**

3c. Apparent capacity degradation in LIBs and SIBs is observed. In contrast, the neat MoS_2 in PIBs realizes the most stable capacity of 170 mAh g^{-1} after 200 cycles with a retention of 94.5% (**Figure 3**d). Although petal-like structures of neat MoS_2 cannot be maintained after 200 times cycling in PIBs (**Figure S14**), the layered structures are remained in large extent with an expanded d-spacing of 7.7 Å after a prolonged cycling. Without protection from the carbon nanofibers, the electrochemical stabilities of MoS_2 show a more striking contrast between the three types of batteries. It is reliable to conclude that MoS_2 intrinsically shows a more stable cyclic performance in PIBs than in LIBs and SIBs.

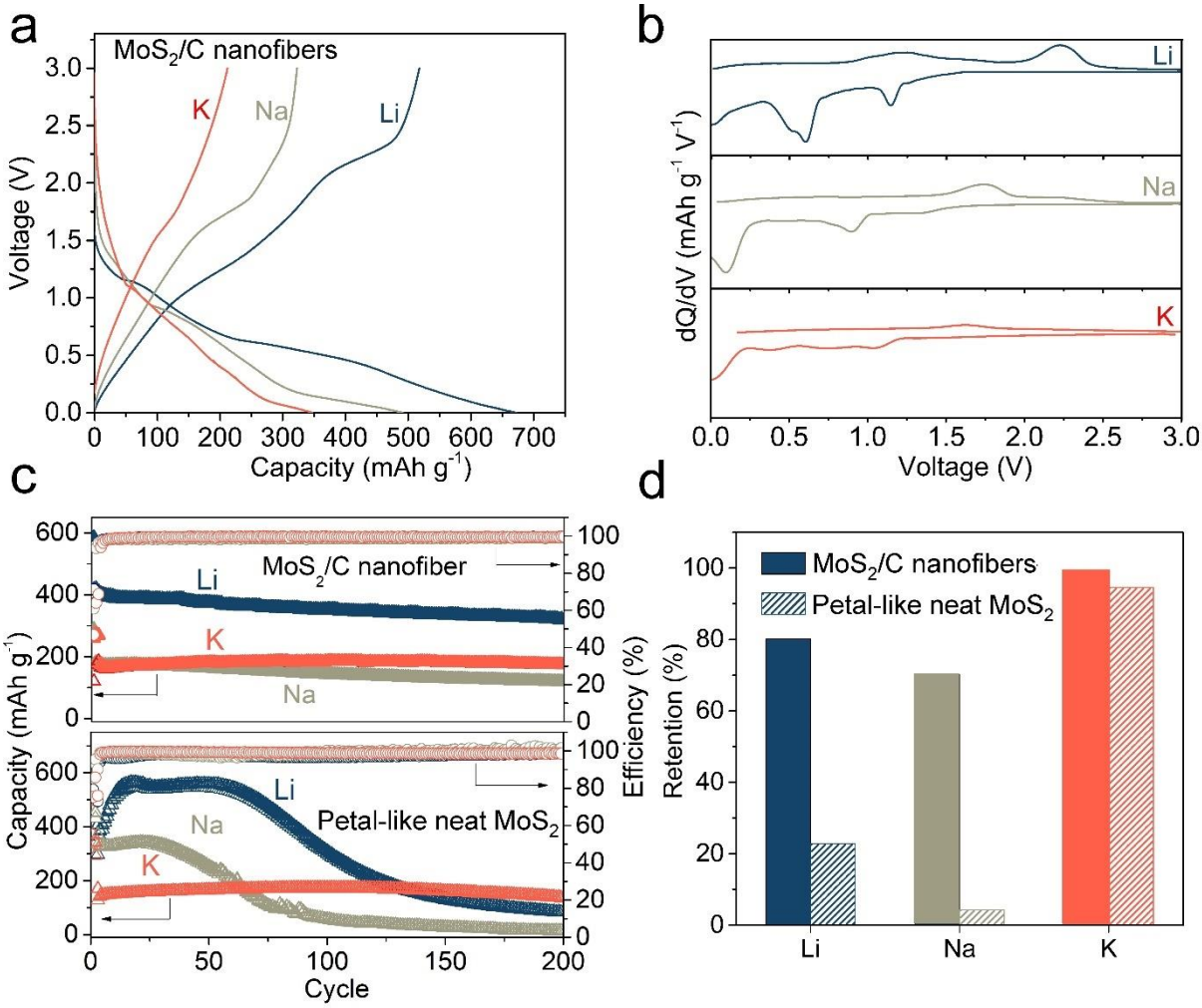

Figure 3. Electrochemical performance in LIBs, SIBs and PIBs. (a) Discharge and charge profiles of MoS_2/C nanofibers at first cycle at 50 m A g^{-1}; (b) dQ/dV vs. voltage plots of MoS_2/C nanofibers at first cycle; (c) Cyclic performance of MoS_2/C nanofibers and petal-like neat MoS_2 at 500 m A g^{-1}; (d) Retention percentage of MoS_2/C nanofibers and neat MoS_2 after 200 cycles.

We further performed *ex situ* TEM to examine the morphologies of MoS_2/C nanofibers cycled 200 times. As shown in **Figure 4**a and inset, all the lamellar structural MoS_2 are disappeared and turned into dense nanoparticles after cycling in LIBs. Those particles can be indexed to the Mo phase with a lattice plane spacing of 2.2 Å (PDF#42-1120), which is one of the conversion products. The layered crystals could no longer be found in SIBs after 200 cycles, and the materials are changed to loose particles with low contrast (**Figure 4**c). The SAED pattern (**Figure 4**c inset) suggests an amorphous phase without prominent diffraction spots or rings, which is possibly amorphous Mo species by inferring from the Li case. Interestingly, many layered crystals with a layer distance of about 7.6 Å are observed in PIBs (**Figure 4**e and inset). There are fewer layered crystals than the first fully discharged one (**Figure 2**f), possibly because part of the layered MoS_2 may be consumed through deep conversion reaction. The reaction schematics are described in **Figure 4**b, d and f: the layered crystals in LIBs/SIBs are easily converted to dense/loose particle structures after long cycles, whereas they are the most stable in PIBs explaining the best cyclic stability in electrochemical tests.

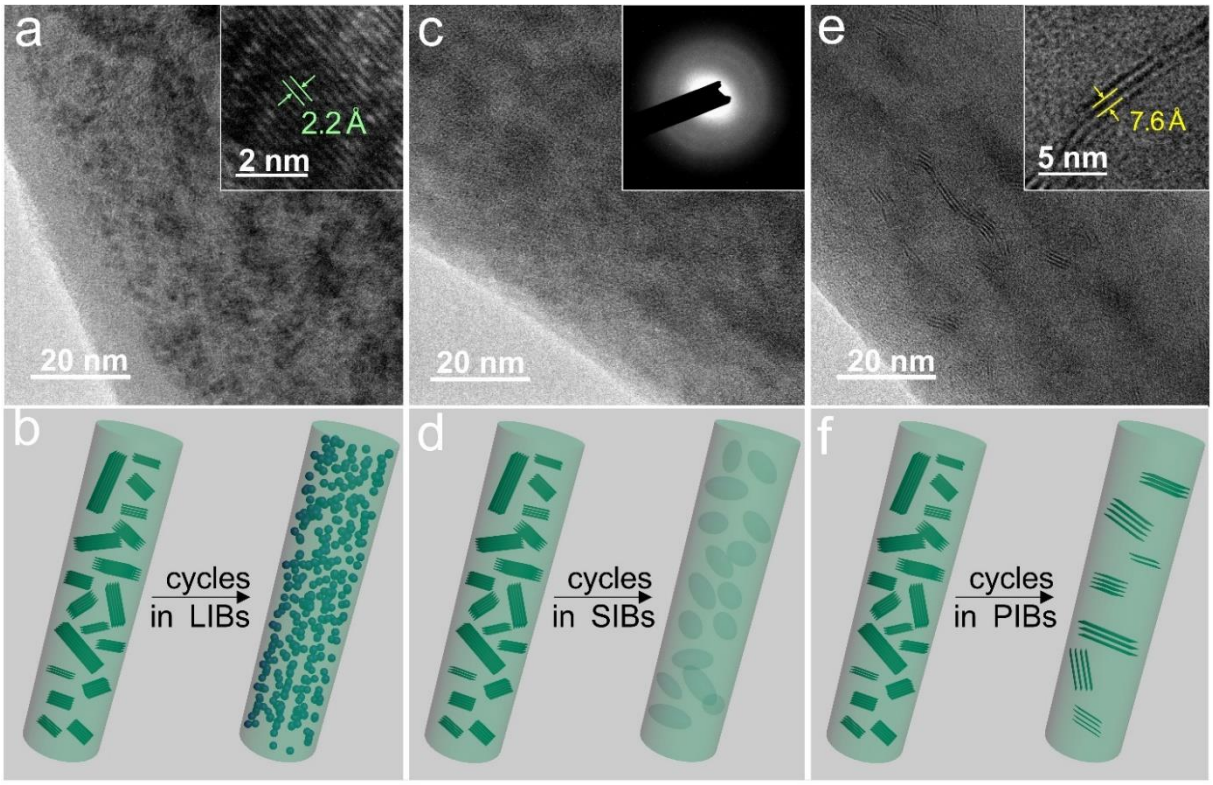

Figure 4. *Ex situ* TEM images and schematics of MoS_2/C nanofibers in (a, b) LIBs, (c, d) SIBs and (e, f) PIBs after 200 cycles.

The exceptional stability upon large K ion insertion suggests different thermodynamic/kinetic processes governing the intercalation and conversion. Density functional theory (DFT) computations were carried out to study the mechanisms. We first calculated the reaction enthalpy of conversion from the intercalated compounds $AMoS_2$ (A represents Li, Na, and K) to A_2S and Mo. Such values could serve as the descriptor of the thermodynamic driving forces for the conversion reactions. We specifically choose the intermediate intercalated compounds as the reference for our calculation because they are the last intercalated compounds before the conversion reaction actually happens in these three systems. The results are shown in **Figure 5**a, **Table S1,** and **Figure S15**a. The decomposition enthalpies of $AMoS_2$ intercalated compounds into Mo and A_2S are -4.46 eV/f.u., -3.16 eV/f.u., and -3.30 eV/f.u. for A=Li, Na, and K,

respectively. This indicates a smaller thermodynamic driving force in the case of K for the conversion to take place, leading to the preservation of a large quantity of the lamellar structures. It is also interesting to note that, within the accuracy of DFT framework (as well as neglecting the temperature effect), all the computed reaction enthalpies are negative, meaning the conversion reactions are energetically favorable to take place even at a pretty low degree of alkalization. Therefore, we speculate that the kinetic factor may play a critical role in the conversion reaction as well since such intercalated compounds are observed in experiments. Due to the lack of reliable methods to directly compute the energy barrier for the complicated phase transition, we analyzed the bond characteristics of $AMoS_2$, which may reflect their easiness of conversion reaction. The charge distributions of $LiMoS_2$, $NaMoS_2$, and $KMoS_2$ are investigated by the charge density difference (**Figure 5**b and **S15**b), which is defined by subtracting the electron densities of Li/Na/K and MoS_2 from the electron density of $LiMoS_2$/$NaMoS_2$/$KMoS_2$. Taking $KMoS_2$ as an example, it is clear in **Figure 5**b that some charges are accumulated between K and S atoms, suggesting their interaction or bonding. To have a better-quantified view, **Figure 5**c and **Figure S16** demonstrates the two-dimensional charge density differences along the planes through Li/Na/K and Mo-S atoms. Interestingly, the charge depletion of Li atom (down to -0.07 e $bohr^{-3}$) is more severe than the one of K atom (down to -0.03 e $bohr^{-3}$). The more polar feature of the charge distribution between Li and S suggests the Li-S bond is more electrovalent than the K-S bond.[49] The polarity is further supported by the Bader analysis (**Figure 5**d and **Table S2-4**) that the Bader charges of alkaline atoms in $LiMoS_2$, $NaMoS_2$, and $KMoS_2$ are +0.87, +0.83 and +0.74 e, respectively. The different polarity between Li/K-S bonds may come from the more dispersed electron cloud of K due to the larger number of electrons. When it comes to the conversion reaction, it is conjectured that the more polar bonds between Li

and S atoms may kinetically facilitate the formation of Li_2S by reducing the charge transfer barrier. Shortly, the conversion reaction in the K-MoS_2 system is suppressed thermodynamically (by the lower formation energy) and kinetically (by the less electrovalent K-S bond).

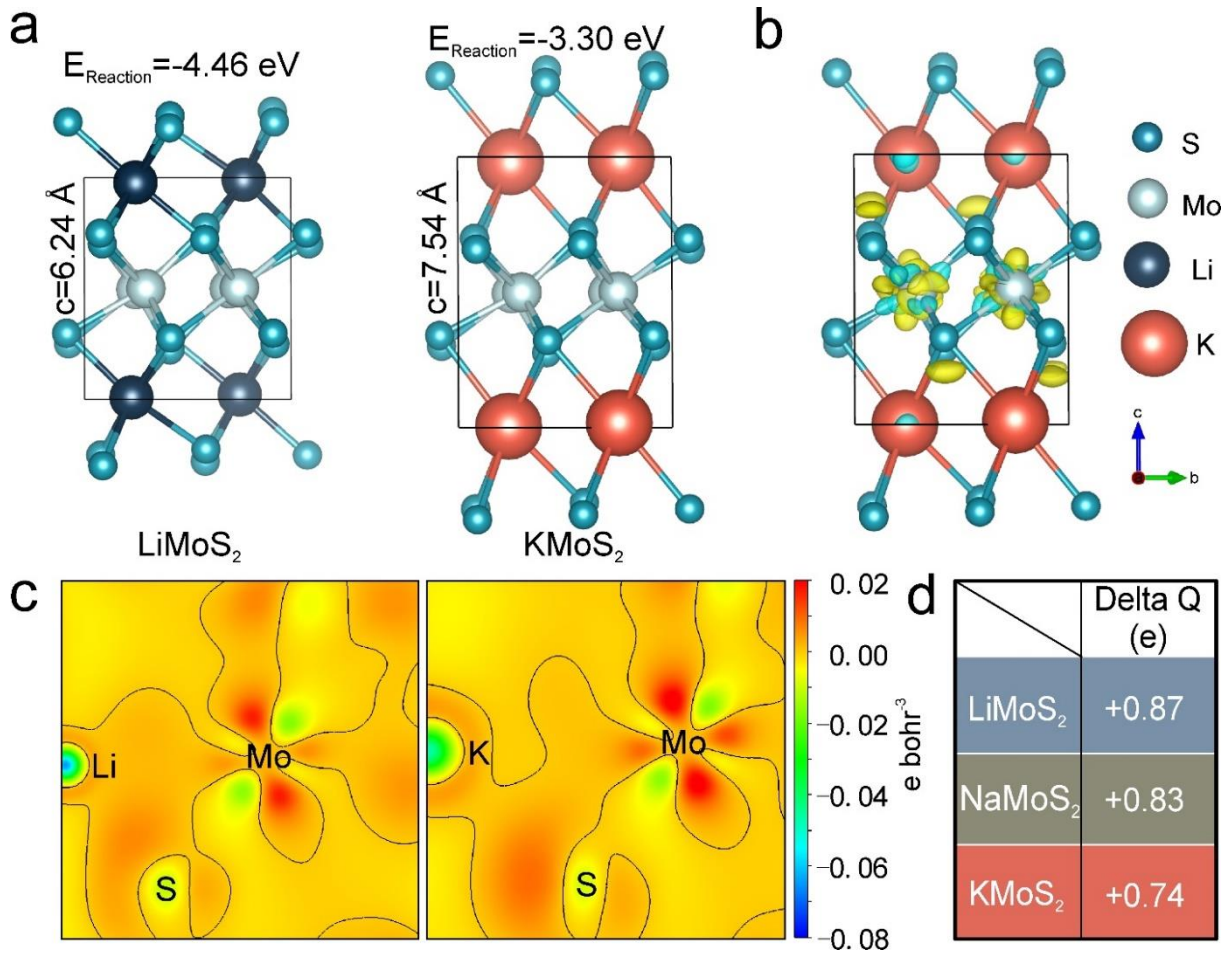

Figure 5. DFT simulations. (a) The calculated structures for $LiMoS_2$ and $KMoS_2$; (b) charge density difference distributions for $KMoS_2$; (c) two-dimensional charge density difference of $LiMoS_2$ and $KMoS_2$ across Li/K and Mo-S; (d) calculated changes in Li/Na/K atoms charges (delta Q) of $LiMoS_2$, $NaMoS_2$ and $KMoS_2$, respectively (a positive value of delta Q indicates charges loss).

Conclusion

The alkali-metal ion storage mechanisms from Li, Na to K case are studied by complementary *in situ* experimental and calculation approaches. We articulate that a massive volume expansion of about 140% occurs in K ion incorporation, but unexpected stability is observed. *In situ* TEM is used to examine the structural evolution of layered MoS_2 upon Li, Na and K ions insertions, indicating that most of the layered crystals are preserved in PIBs. Detailed reaction paths are elucidated by *in situ* XRD and *ex situ* TEM. It is revealed that a large ratio of intercalation reaction occurs during K ions uptake, giving rise to better structural and electrochemical stability than Li and Na ions insertion. Layered MoS_2 tends to be transformed into tiny particles by deep conversion reaction in the cases of LIBs and SIBs. Assisted by the DFT calculations, we unveil the thermodynamic and kinetic origins of the anomalous stability in the insertion of K ions, where relies on the less electrovalent of K-S bond arising from the larger dispersed electron clouds of K atom than Li and Na ones.

Experimental section

Preparation of MoS_2/C nanofibers, carbon nanofibers and petal-like neat MoS_2

MoS_2/C nanofibers were prepared by electrospinning. Typically, polyacrylonitrile (PAN, 0.5 g) was dissolved in dimethylformamide (DMF, 10 mL). Ammonium tetra-thiomolybdate ($(NH_4)_2MoS_4$, 0.8 g) was added under continuous stirring to get a uniform solution. Electrospinning was conducted under a high voltage of 18 kV with a feed rate of 30 μL min^{-1} to obtain a film on Al foils. The film precursor was first stabilized at 250 ºC for 4 hours in a Muffle furnace before annealing at 900 ºC for 2 hours under argon atmosphere. After the annealing, $(NH_4)_2MoS_4$ decomposed to MoS_2, and PAN turn into carbon. The pure carbon nanofibers were prepared by the same method without adding $(NH_4)_2MoS_4$. In comparison, petal-like neat MoS_2 was synthesized by a hydrothermal method.[50] Ammonium heptamolybdate tetrahydrate

($(NH_4)_6Mo_7O_{24}\cdot 4H_2O$, 0.5 mmol) and thiourea (NH_2CSNH_2, 7 mmol) were dissolved in deionized (DI, 35 mL) water. The solution was kept in a 50 mL Teflon-lined stainless steel autoclave at 220 ºC for 18 hours. The final product was washed by DI water and ethanol before drying at 80 ºC overnight.

Electrochemical performance measurement

All cells were assembled *via* two-electrode CR2032 coin half-cell in Argon-filled glovebox. MoS_2/C nanofibers and carbon nanofibers were used as freestanding electrodes in batteries tests. Neat MoS_2 electrodes were mixed with vapor grown carbon fibers (VGCF), carbon black (Super P) and carboxymethyl cellulose (CMC) at a mass ratio of 7: 1: 1: 1 to make a tape on Cu current collector and dried at 80 ºC overnight under vacuum. 1 M $LiPF_6$ in ethylene carbonate (EC)/ dimethyl carbonate (DMC) with a volume ratio of 1:1, 1 M $NaPF_6$ in propylene carbonate (PC) with 3 vol.% FEC and 1 M potassium bis(fluorosulfony)imide (KFSI) in EC/PC (volume ratio of 1:1) were adopted as electrolytes for LIB, SIB, and PIB, respectively. Glass fiber membranes (Whatman, GF/D) were used as separators. All batteries were tested on LAND battery test system.

Characterizations

The X-ray powder diffraction (XRD) patterns were collected by Rigaku Smartlab with Cu-Kα radiation source at 45 kV and 200 mA condition. For *in situ* XRD measurements, an XRD cell with a beryllium window was employed. The morphologies of MoS_2/C nanofibers were examined on scanning electron microscopes (SEM, JEOL JSM-6335F). Thermogravimetric analysis (TGA) was conducted using TGA/DSC3+ (Mettler Toledo) from 50 to 650 °C with a heating rate of 15 °C·min^{-1} in air. X-ray photoelectron spectroscopy (XPS) are performed on Thermo Scientific Nexsa. TEM and scanning TEM (STEM) were performed using JEOL JEM-

2100F TEM/STEM operated at 200 kV, equipped with a Gatan Enfina electron spectrometer. For the *in situ* TEM study, the MoS_2/C nanofibers were loaded onto electrochemical etched micro-size tungsten tip and fixed with conductive silver epoxy. Another tungsten tip with submicron size at the top was used to scratch fresh alkaline metal (Li, Na, or K) surface in an argon-filled glove box and attached to a piezo-driven biasing probe built the Nanofactory TEM scanning tunneling microscopy (TEM-STM) holder. Once the sealed holder was taken out from the glovebox, it was inserted into the TEM column as quickly as possible for immediate *in situ* study by TEM. The native A_2O (A represents Li, Na or K) on the alkaline metal surface was severed as a solid electrolyte. The voltage bias between alkaline metal tip and MoS_2 tip was applied to -5 V, which was higher than those applied in coin cells. It was necessary to use a slightly higher potential in *in situ* TEM measurements to drive alkaline ions (Li^+, Na^+ and K^+) through the solid electrolytes due to the poor ionic conductivity of solid electrolytes and high resistance between these two electrodes.[45] In this case, the driving force in *in situ* TEM might be larger than those in coin cells but didn't show effective changes by comparing with the *ex situ* TEM results.[51, 52] Therefore, the *in situ* TEM results were reliable. The three *in situ* videos were taken on 200, 250 and 100 kX magnification for Li, Na and K with 0.5 s exposure time, respectively. The corresponding dose rate for Li, Na, and K system (units of the number of electrons per square angstrom per second, $e^- Å^{-2} s^{-1}$) was recorded and calibrated, equaled to 443, 764 and 122 $e^- Å^{-2} s^{-1}$, respectively. The *ex situ* TEM samples were prepared by disassembling the coin cell in the glovebox and washing with dimethyl carbonate (DMC) to remove the residue electrolyte.

DFT simulations

DFT calculations were conducted under the generalized gradient approximation (GGA) parameterized by Perdew-Burker-Ernzerhof (PBE) performed in the Vienna Ab initio Simulation

Package (VASP).[53-55] To account for the van der Waals interactions, the optimized PBE functional was applied.[56] The energy cutoff for plane-wave basis set was 500 eV, while the k-point was sampled with a spacing of less than 0.05 $Å^{-1}$. The convergence criteria for electron self-consistency and force were 10^{-6} eV and 0.02 eV $Å^{-1}$, respectively.

Conflicts of interest

The authors declare no competing financial interests.

Acknowledgements

This work is supported by the Hong Kong Research Grants Council through the General Research Fund (Project No. 15305219), the Key Project for Basic Research of Shenzhen (No. JCYJ20170818104125570), and the Hong Kong Polytechnic University (ZVRP, and 1-ZE30).

Notes and references

1 D. Larcher and J. M. Tarascon, *Nat. Chem.*, 2015, **7**, 19-29.
2 K. Chayambuka, G. Mulder, D. L. Danilov and P. H. L. Notten, *Adv. Energy Mater.*, 2018, **8**, 1800079.
3 J. Y. Hwang, S. T. Myung and Y. K. Sun, *Adv. Funct. Mater.*, 2018, **28**, 1802938.
4 H. Tan, X. Lin, J. Huang, J. Huang, M. Shi, X. Du and B. Zhang, *Nanoscale*, 2019, **11**, 11445-11450.
5 J. Xu, Y. Dou, Z. Wei, J. Ma, Y. Deng, Y. Li, H. Liu and S. J. A. S. Dou, *Adv. Sci.*, 2017, **4**, 1700146.
6 Z. X. Wei, D. X. Wang, M. L. Li, Y. Gao, C. Z. Wang, G. Chen and F. Du, *Adv. Energy Mater.*, 2018, **8**, 1801102.
7 D. Ni, W. Sun, Z. Wang, Y. Bai, H. Lei, X. Lai and K. Sun, *Adv. Energy Mater.*, 2019, **9**, 1900036.
8 J. Zheng, Y. Yang, X. Fan, G. Ji, X. Ji, H. Wang, S. Hou, M. R. Zachariah and C. Wang, *Energy Environ. Sci.*, 2019, **12**, 615-623.
9 L. Ji, M. Gu, Y. Shao, X. Li, M. H. Engelhard, B. W. Arey, W. Wang, Z. Nie, J. Xiao, C. Wang, J. G. Zhang and J. Liu, *Adv. Mater.*, 2014, **26**, 2901-2908.
10 W. Zhang, Z. Wu, J. Zhang, G. Liu, N.-H. Yang, R.-S. Liu, W. K. Pang, W. Li and Z. Guo, *Nano Energy*, 2018, **53**, 967-974.
11 X. Y. Lin, X. Q. Du, P. S. Tsui, J. Q. Huang, H. Tan and B. Zhang, *Electrochim. Acta*, 2019, **316**, 60-68.

12 Z. L. Jian, Z. Y. Xing, C. Bommier, Z. F. Li and X. L. Ji, *Adv. Energy Mater.*, 2016, **6**, 1501874.
13 X. Lin, J. Huang and B. Zhang, *Carbon*, 2019, **143**, 138-146.
14 Z. Liu, Y.-Y. Hu, M. T. Dunstan, H. Huo, X. Hao, H. Zou, G. Zhong, Y. Yang and C. P. Grey, *Chem. Mater.*, 2014, **26**, 2513-2521.
15 X. Lin, J. Huang, H. Tan, J. Huang and B. Zhang, *Energy Storage Mater.*, 2019, **16**, 97-101.
16 B. Zhang, R. Dugas, G. Rousse, P. Rozier, A. M. Abakumov and J. M. Tarascon, *Nat Commun*, 2016, **7**, 10308.
17 K. Mizushima, P. Jones, P. Wiseman and J. B. Goodenough, *J Materials Research Bulletin*, 1980, **15**, 783-789.
18 N. Yabuuchi, K. Kubota, M. Dahbi and S. Komaba, *Chem. Rev.*, 2014, **114**, 11636-11682.
19 A. Darwiche, C. Marino, M. T. Sougrati, B. Fraisse, L. Stievano and L. Monconduit, *J. Am. Chem. Soc.*, 2012, **134**, 20805-20811.
20 H. Kim, J. C. Kim, M. Bianchini, D. H. Seo, J. Rodriguez-Garcia and G. Ceder, *Adv. Energy Mater.*, 2018, **8**, 1702384.
21 J. Q. Huang, X. Y. Lin, H. Tan and B. Zhang, *Adv. Energy Mater.*, 2018, **8**, 1703496.
22 F. Xie, L. Zhang, B. Chen, D. Chao, Q. Gu, B. Johannessen, M. Jaroniec and S.-Z. Qiao, *Matter*, 2019, **1**, 1681-1693.
23 Q. Zhang, J. Mao, W. K. Pang, T. Zheng, V. Sencadas, Y. Chen, Y. Liu and Z. Guo, *Adv. Energy Mater.*, 2018, **8**, 1703288.
24 T. Wang, S. Chen, H. Pang, H. Xue and Y. Yu, *Adv. Sci.*, 2017, **4**, 1600289.
25 J. Wang, J. Liu, D. Chao, J. Yan, J. Lin and Z. X. Shen, *Adv. Mater.*, 2014, **26**, 7162-7169.
26 L. David, R. Bhandavat and G. Singh, *ACS Nano*, 2014, **8**, 1759-1770.
27 Y. Wang, L. Yu and X. W. Lou, *Angew. Chem. Int. Ed. Engl.*, 2016, **55**, 7423-7426.
28 Y. Fang, D. Luan, Y. Chen, S. Gao and X. W. D. Lou, *Angew. Chem. Int. Ed. Engl.*, 2020, **59**, 7178-7183.
29 M. Han, Z. Lin and J. Yu, *Journal of Materials Chemistry A*, 2019, **7**, 4804-4812.
30 Z. Li, K. Jiang, F. Khan, A. Goswami, J. Liu, A. Passian and T. J. S. a. Thundat, 2019, **5**, eaav2820.
31 L. Zhang, D. Sun, J. Kang, J. Feng, H. A. Bechtel, L. W. Wang, E. J. Cairns and J. Guo, *Nano Lett.*, 2018, **18**, 1466-1475.
32 X. Q. Du, J. Q. Huang, X. Y. Guo, X. Y. Lin, J. Q. Huang, H. Tan, Y. Zhu and B. Zhang, *Chem. Mater.*, 2019, **31**, 8801-8809.
33 X. Wang, X. Shen, Z. Wang, R. Yu and L. Chen, *ACS Nano*, 2014, **8**, 11394-11400.
34 J. Ge, L. Fan, J. Wang, Q. Zhang, Z. Liu, E. Zhang, Q. Liu, X. Yu and B. J. A. E. M. Lu, 2018, **8**, 1801477.
35 B. R. Jia, Q. Y. Yu, Y. Z. Zhao, M. L. Qin, W. Wang, Z. W. Liu, C. Y. Lao, Y. Liu, H. W. Wu, Z. L. Zhang and X. H. Qu, *Adv. Funct. Mater.*, 2018, **28**, 1803409.
36 G. K. Veerasubramani, M.-S. Park, G. Nagaraju and D.-W. Kim, *Journal of Materials Chemistry A*, 2019, **7**, 24557-24568.
37 L. Wang, Z. Xu, W. Wang and X. Bai, *J. Am. Chem. Soc.*, 2014, **136**, 6693-6697.
38 F. X. Li, J. L. Zou, L. J. Cao, Z. Q. Li, S. Gu, Y. Liu, J. Q. Zhang, H. T. Liu and Z. G. Lu, *J. Phys. Chem. C*, 2019, **123**, 5067-5072.

39 A. Andersen, S. M. Kathmann, M. A. Lilga, K. O. Abrecht, R. T. Hallen and D. H. Mei, *J. Phys. Chem. C*, 2012, **116**, 1826-1832.
40 P. Gao, L. Wang, Y. Zhang, Y. Huang and K. Liu, *ACS Nano*, 2015, **9**, 11296-11301.
41 B. Chen, H. Lu, J. Zhou, C. Ye, C. Shi, N. Zhao and S.-Z. Qiao, *Adv. Energy Mater.*, 2018, **8**, 1702909.
42 S. Hao, X. Shen, M. Tian, R. C. Yu, Z. X. Wang and L. Q. Chen, *Nano Energy*, 2017, **41**, 217-224.
43 K. Leng, Z. Chen, X. Zhao, W. Tang, B. Tian, C. T. Nai, W. Zhou and K. P. Loh, *ACS Nano*, 2016, DOI: 10.1021/acsnano.6b05746, 9208-9215.
44 Z. Zhu, Y. Tang, W. R. Leow, H. Xia, Z. Lv, J. Wei, X. Ge, S. Cao, Y. Zhang, W. Zhang, H. Zhang, S. Xi, Y. Du and X. Chen, *Angew. Chem. Int. Ed. Engl.*, 2019, **58**, 3521-3526.
45 Z. Fan, L. Zhang, D. Baumann, L. Mei, Y. Yao, X. Duan, Y. Shi, J. Huang, Y. Huang and X. Duan, *Adv. Mater.*, 2019, **31**, e1900608.
46 W. Wang, B. Jiang, C. Qian, F. Lv, J. Feng, J. Zhou, K. Wang, C. Yang, Y. Yang and S. Guo, *Adv. Mater.*, 2018, **30**, 1801812.
47 H. Huang, J. Cui, G. Liu, R. Bi and L. Zhang, *ACS Nano*, 2019, **13**, 3448-3456.
48 P. Xiong, J. Wu, M. Zhou and Y. Xu, *ACS Nano*, 2020, **14**, 1018-1026.
49 H. L. Li, K. Yu, H. Fu, B. J. Guo, X. Lei and Z. Q. Zhu, *J. Phys. Chem. C*, 2015, **119**, 7959-7968.
50 S. Zhang, B. V. Chowdari, Z. Wen, J. Jin and J. Yang, *ACS Nano*, 2015, **9**, 12464-12472.
51 M. T. McDowell, S. W. Lee, J. T. Harris, B. A. Korgel, C. Wang, W. D. Nix and Y. Cui, *Nano Lett.*, 2013, **13**, 758-764.
52 Y. Wu, S. Hu, R. Xu, J. Wang, Z. Peng, Q. Zhang and Y. Yu, *Nano Lett.*, 2019, **19**, 1351-1358.
53 P. E. Blochl, *Phys. Rev. B*, 1994, **50**, 17953-17979.
54 G. Kresse and J. Furthmuller, *Phys. Rev. B*, 1996, **54**, 11169-11186.
55 J. P. Perdew, K. Burke and M. Ernzerhof, *Phys. Rev. Lett.*, 1996, **77**, 3865-3868.
56 J. Klimes, D. R. Bowler and A. Michaelides, *J. Phys.: Condens. Matter*, 2010, **22**, 022201.